Two-Color Coherent Control of Femtosecond Above-Threshold Photoemission from a Tungsten Nanotip

Michael Förster,[1,2,*] Timo Paschen,[1] Michael Krüger,[1,2,†] Christoph Lemell,[3] Georg Wachter,[3] Florian Libisch,[3] Thomas Madlener,[3] Joachim Burgdörfer,[3] and Peter Hommelhoff[1,2,4]

[1]*Department of Physics, Friedrich-Alexander-Universität Erlangen-Nürnberg (FAU), Staudtstraße 1, 91058 Erlangen, Germany*
[2]*Max Planck Institute of Quantum Optics, Hans-Kopfermann-Straße 1, 85748 Garching, Germany*
[3]*Institute for Theoretical Physics, Vienna University of Technology, Wiedner Hauptstraße 8-10, 1040 Vienna, Austria*
[4]*Max Planck Institute for the Science of Light, Staudtstraße 2, 91058 Erlangen, Germany*

(Received 4 March 2016; revised manuscript received 9 August 2016; published 14 November 2016)

We demonstrate coherent control of multiphoton and above-threshold photoemission from a single solid-state nanoemitter driven by a fundamental and a weak second harmonic laser pulse. Depending on the relative phase of the two pulses, electron emission is modulated with a contrast of the oscillating current signal of up to 94%. Electron spectra reveal that all observed photon orders are affected simultaneously and similarly. We confirm that photoemission takes place within 10 fs. Accompanying simulations indicate that the current modulation with its large contrast results from two interfering quantum pathways leading to electron emission.

DOI: 10.1103/PhysRevLett.117.217601

Ionization by two-color laser fields with well-defined relative phase allows one to tune and control electronic dynamics on the (sub)femtosecond time scale. By virtue of the synthesized laser field, the energy and angular distributions of emitted electrons can be manipulated. Two-color pulses have been used in investigations of above-threshold ionization of atoms [1–3], controlled dissociative ionization [4–6], dichroism in ionization [7,8], and orientation of molecules [9]. Recently, they have also been applied to control interference fringes in the momentum distribution of electron emission [10–12]. In this Letter we demonstrate exquisite coherent emission control by simultaneous interaction of fundamental (ω) and second harmonic (2ω) femtosecond laser pulses with condensed matter. Specifically, we control photoemission from an individual nanotip.

While nanotips are nowadays routinely used as electron sources in high-resolution electron microscopes [13], their superb transverse coherence known from dc field emission has only recently been observed in photoemission [14]. Field enhancement at the apex of nanotips [15] confines and enhances electron emission, thus enabling the study of strong-field physics with moderate laser intensities well below the damage threshold [16–21]. Laser-induced photoemission from tips (for extensive reviews, see Ref. [22]) has already been employed in pulsed electron guns for electron diffraction experiments [23,24], while arrays of nanotips have been fabricated and explored as electron sources for compact coherent x-ray production [25–27]. Recently, a $\omega - 2\omega$ experiment was performed on a silicon tip array, but no phase-resolved signal indicative of coherent control was reported [27].

In our experiment, atomic-scale *in situ* control over the sample surface results in a well-defined nanoemitter that surpasses the limitations of focal averaging and inhomogeneous broadening. We show that electron emission induced by a strong fundamental pulse can be enhanced or suppressed with a contrast of up to 94% when superimposing a weak second harmonic pulse. This scheme thereby allows efficient coherent control of the nanotip photocurrent utilizing the metal-vacuum interface to suppress emission in one direction. Accompanying simulations suggest that the strong modulation can be explained in terms of two nearly perfectly constructively or destructively interfering quantum pathways, each individually leading to electron emission.

We generate phase-locked pairs of fundamental and second harmonic pulses by passing the output of an Er^{3+}-doped femtosecond fiber laser through a 100 μm thick β-barium borate (BBO) crystal (Fig. 1). Central wavelengths and pulse durations are 1560 nm and 74 fs for the fundamental and 780 nm and 64 fs for the second harmonic. The pulses are sent into a Mach-Zehnder interferometer with dichroic beam splitters where the delay (or, equivalently, the relative optical phase) between the pulses can be varied by up to 2 ps by a piezoelectric actuator and locked within this range [28]. The phase between the two colors is not measured in our experiment. A half-wave plate in the 2ω arm rotates the 2ω polarization to align it with the ω polarization and the tip axis, unless stated otherwise. Intensities can be adjusted independently by neutral density filter wheels. The laser pulses are directed into a UHV chamber and focused onto a [310]-oriented tungsten nanotip with a nominal work function of $W_0 = 4.31$ eV [29]. With the applied bias voltage, an effective barrier height of $W \approx 3.6$ eV results. The tips employed in the experiments display radii of curvature around 10 nm, determined *in situ* by field ion microscopy [30] (see Supplemental Material (SM) for details [31]).

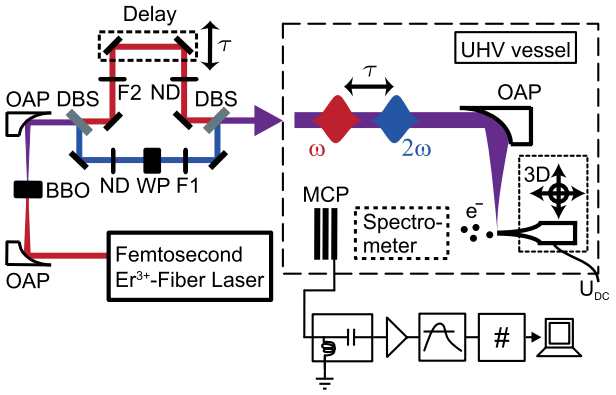

FIG. 1. Experimental setup. The second harmonic of Er^{3+}-doped fiber laser pulses is generated in BBO using off-axis parabolas (OAPs) for dispersion-free focusing and collimation. Beams enter a Mach-Zehnder interferometer with dichroic beam splitters (DBS), where the fundamental passes a variable delay stage. Intensities are independently controlled with neutral density filter wheels (ND) and the beams are spectrally filtered (F1, F2). The polarization of the second harmonic is rotated with a half-wave plate (WP). After recombination of the two pulses with variable time delay τ, they are focused onto a tungsten tip with an off-axis parabola. Electrons are detected on a microchannel plate (MCP) or with a spectrometer using single electron pulse counting.

Photoelectrons from the biased tip are either counted directly at a microchannel plate (MCP) detector or, alternatively, pass an energy high-pass filter and are only then detected by a MCP, enabling spectrally-resolved measurements.

Typical peak near-field intensities at the tip's apex are on the order of $I_\omega = 3 \times 10^{11}$ W/cm^2 for the fundamental and $I_{2\omega} = 7 \times 10^9$ W/cm^2 for the second harmonic, including field enhancement [39,40] (see SM for details [31]). The near fields of both colors result in electron emission in the multiphoton regime with minimum Keldysh parameters, $\gamma = \sqrt{W_0/2U_p}$ of $\gamma_{\omega,\mathrm{min}} = 2.7$ and $\gamma_{2\omega,\mathrm{min}} = 47$, where U_p is the ponderomotive energy. The second harmonic is much weaker than the fundamental with the ratio of second harmonic to fundamental near-field peak intensity $I_{2\omega}/I_\omega \leq 4\%$. Electron emission induced exclusively by a pulse at frequency ω is observed to be at least more than 1 order of magnitude larger than electron emission by a 2ω pulse.

In regions of temporal overlap of the ω and 2ω pulses, we observe a dramatic change in the emission characteristics: The emitted current strongly oscillates as a function of the delay [central region of Fig. 2(a), magnified in Fig. 2(b)]. This behavior is well described by a sine fit (red solid line). The contrast is up to 94%; i.e., electron emission is either drastically enhanced or reduced to almost zero as compared to the emission from the tip for separated pulses. Despite the weak 2ω intensity admixture of 2%, the maximum achievable electron current is almost 4 times the current for separated pulses for these parameters.

For further analysis, we Fourier transform the data of Fig. 2(a) and obtain the spectrum shown in Fig. 2(c). On top of a white-noise background, the Fourier spectra for overlapping pulses feature two main peaks: a low-frequency (dc) component in region of interest 0 (ROI 0) and a component at finite frequency (ROI 1) peaking at 390 THz, the frequency of the second harmonic. A windowed inverse Fourier transform of the data in ROI 0 and ROI 1 and an additional Hilbert transform of the data in ROI 1 to obtain its envelope yield the temporal variation of the amplitude of the ROI 0 and ROI 1 components as a function of the delay τ [Fig. 2(d)]. These can be well approximated by Gaussian fits, $G_i(\tau) = A_i + B_i \exp(-4 \ln 2\tau^2/\Delta_i^2)$. Here $i = 0, 1$ for ROI 0 and ROI 1, τ denotes the $\omega - 2\omega$ delay, and Δ_i are the full widths at half maximum of the photocurrent components. The ROI amplitude fit parameters B_i serve as direct measure of the cooperative effects in the region of temporal overlap.

We find that B_0 and B_1 scale differently with the second harmonic intensity $I_{2\omega}$. While B_0 increases linearly with $I_{2\omega}$, B_1 shows a $\sqrt{I_{2\omega}}$ dependence [Fig. 2(e)]. The contrast of the oscillating current signal, i.e., its visibility,

$$V = \frac{N_{\mathrm{max}} - N_{\mathrm{min}}}{N_{\mathrm{max}} + N_{\mathrm{min}}}, \tag{1}$$

determined from sine fits, reaches up to 94% for an intensity admixture of the 2ω component of 2% to the fundamental near-field intensity of $I_\omega = 330$ GW/cm^2 [Fig. 2(e)]. With the emergence of higher-order contributions (additional Fourier component at 4ω) for admixtures of 4% the second harmonic cannot be regarded a weak perturbation any longer. We therefore exclude the data point at $I_{2\omega} = 14$ GW/cm^2 from the following analysis.

The cooperative electron emission also varies as a function of the orientation of the incident polarization vector of the second harmonic pulse [Fig. 2(f)]. The maximum cooperative effect is found for the 2ω polarization aligned with the ω component, which is parallel to the tip axis. Rotating the incident 2ω polarization vector the cooperative electron emission is reduced and reaches its minimum for the 2ω polarization perpendicular to the tip axis. This is expected as the near field excited at the apex by the 2ω field is strongest for an incident polarization aligned with the tip axis and also overlaps best with the near field excited by the fundamental. Further, for an incident polarization vector orthogonal to the tip axis, its enhanced region is moved away from the tip apex [41], and thus away from the low-work-function (310) plane.

To gain further insight into the underlying processes, we have recorded electron-energy spectra when either one of the two pulses is blocked or both are simultaneously present; see Fig. 3. With only the 2ω pulse on target (blue line), we observe just a weak two-photon emission current. By contrast, with only the fundamental pulse

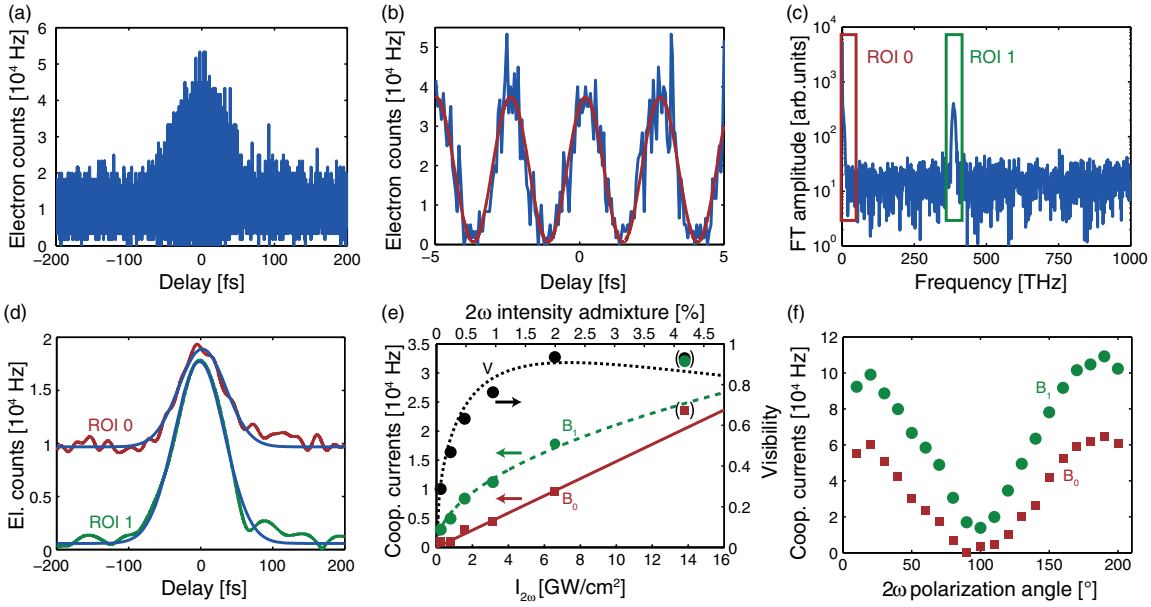

FIG. 2. Demonstration of coherent control of the photocurrent. (a) Electron current as a function of delay τ between ω and 2ω pulse for $I_\omega = 330$ GW/cm^2 and $I_{2\omega} = 6.6$ GW/cm^2. For positive values of delay the 2ω pulse encounters the tip first. We define $\tau = 0$ at a current maximum in temporal overlap. (b) Magnification of the central area of (a). A sine fit to the data is shown as red solid line. (c) Absolute value of the Fourier transform (FT) of the data in (a). The cooperative photocurrent consists almost exclusively of an oscillatory component at 2ω (ROI 1) and a dc component (ROI 0). (d) Inverse Fourier transform (IFT) of data in ROI 0 and IFT and Hilbert transform of data in ROI 1. Gaussian fits to the data are shown in blue. (e) ROI amplitude fit parameters B_0 and B_1 as a function of the second harmonic intensity for a fundamental intensity of $I_\omega = 330$ GW/cm^2. B_0 and B_1 are proportional to $I_{2\omega}$ (red solid line) and $\sqrt{I_{2\omega}}$ (green dashed line), respectively. The contrast (visibility) of the current oscillation calculated using Eq. (1) (black dots) and Eq. (5) (black dotted line) reaches up to 94% in this experiment. (f) B_0 (red squares) and B_1 (green dots) as a function of the rotation angle θ of the polarization direction of the second harmonic with respect to the tip axis and the fundamental field for $I_\omega = 410$ GW/cm^2 and $I_{2\omega} = 13$ GW/cm^2.

present (black line), a typical above-threshold photoemission spectrum containing many orders appears [17]. Overlapping ω and 2ω pulses can homogeneously suppress or enhance emission for the pulse delay locked to minimum (green) or maximum (red) of total photocurrent. For quantitative analysis of the two-color emission, we decompose the total emission rate $R_{\mathrm{tot}} = \sum_n r_n$ and record the individual emission rates r_n of several multiphoton orders n as a function of the two-color phase ϕ. We fit them with sinusoidal fits of the form $r_n(\phi) = C_n + D_n \cos(\phi + \phi_n)$. We thus obtain individual visibilities $V_n = D_n/C_n$ and phase offsets ϕ_n. Our results show that the emission rates of all multiphoton orders vary sinusoidally with the two-color phase, have the same visibility corresponding to the overall photocurrent visibility, and display no relative phase offset (see Sec. II of SM for details [31]).

Therefore, the total emitted current can be described by just two effective emission pathways (see Sec. III of SM [31]). The emitted current from fundamental alone ($\approx A_0$) scales with I_ω^4 despite the presence of higher photon orders. Thus, effective emission pathway 1 with rate R_1 corresponds to the absorption of four photons of the fundamental. Effective pathway 2 involves the absorption of two photons of the fundamental and one photon of the second harmonic resulting in electron emission with rate R_2. Thereby, the second harmonic is treated as a (lowest-order) perturbation. The interference term between the two paths R_{12} oscillates with the relative phase between the pathways, $\phi(\tau) = \phi_{2\omega} - 2\phi_\omega - \phi_e$, which we control via the adjustable pulse delay τ. ϕ_e denotes the unknown phase relation of the electronic states connected by the optical transition. It is noteworthy that our model is reminiscent of heterodyning.

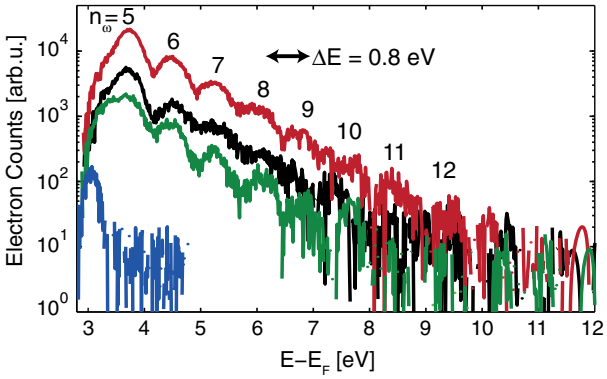

FIG. 3. Experimental electron spectra for $I_\omega = 410$ GW/cm^2 and $I_{2\omega} = 13$ GW/cm^2. Blue: 2ω pulse alone. Black: ω pulse alone. Red: ω and 2ω pulses with relative phase locked at photocurrent maximum. Green: ω and 2ω pulses with relative phase locked at photocurrent minimum.

It is easy to see that this model predicts the following dependencies on the intensities:

$$R_1 = \alpha^4 I_\omega^4, \tag{2}$$

$$R_2 = \alpha^2 I_\omega^2 \beta I_{2\omega}, \tag{3}$$

$$R_{12} = 2\sqrt{R_1 R_2}\cos\phi = 2\alpha^3 I_\omega^3 \sqrt{\beta I_{2\omega}}\cos\phi, \tag{4}$$

where α and β are proportionality factors for the absorption of ω and 2ω photons, respectively. We identify the cooperative contribution to B_0 with pathway R_2 and the amplitude of the oscillation B_1 with R_{12}.

The parameters α and β can be extracted by comparing our experimental data with the quantum-pathway interference model introduced above. Evaluating R_1 using the observed count rate with the fundamental alone at $I_\omega = 330\ \mathrm{GW/cm^2}$, we find $\alpha^4 = (8.068 \pm 0.080) \times 10^{-43}\ \mathrm{Hz\,cm^8\,W^{-4}}$. Evaluating R_2 to extract $\alpha^2\beta$ from the scaling of B_0 with second harmonic intensity in Fig. 2(e) yields $\alpha^2\beta = (1.22 \pm 0.15) \times 10^{-29}\ \mathrm{Hz\,cm^6\,W^{-3}}$. From these results for α^4 and $\alpha^2\beta$ we can directly obtain the prefactor for the interference term R_{12}, yielding $2\alpha^3\sqrt{\beta} = (6.27 \pm 0.38) \times 10^{-36}\ \mathrm{Hz\,cm^7\,W^{-3.5}}$. This factor can also be derived independently from the scaling of B_1 with $I_{2\omega}$ [Fig. 2(e)], which yields $2\alpha^3\sqrt{\beta} = (5.70 \pm 0.52) \times 10^{-36}\ \mathrm{Hz\,cm^7\,W^{-3.5}}$. The excellent agreement between the two independently obtained values for $2\alpha^3\sqrt{\beta}$ is a strong indication that our simple model captures the essential features of the two-color ionization process well.

We can, furthermore, evaluate the visibility of the interference fringes:

$$V(I_\omega, I_{2\omega}) = \frac{R_{12}}{R_1 + R_2} = \frac{2\alpha^3 I_\omega^3 \sqrt{\beta I_{2\omega}}}{\alpha^4 I_\omega^4 + \alpha^2 I_\omega^2 \beta I_{2\omega}}. \tag{5}$$

Figure 2(e) shows the visibility $V(I_\omega, I_{2\omega})$ calculated using the quantum-pathway interference model (black dotted line) together with the experimental data points [Eq. (1)]. Again, excellent agreement between the model and the experimental data is found.

Both a simple tunneling model and a 1D jellium time-dependent density functional theory simulation [19] predict a strong current modulation with phase delay but fail to describe the sinusoidal shape observed in the experiment (see Sec. V of SM for details [31]). In a 3D ground-state density functional theory calculation for the W(310) surface, we observe a strong modulation of the local density of states (LDOS) below the vacuum level compared to the smooth $\rho \propto \sqrt{E}$ of the jellium model (Fig. 4; see SM for details [31]). Of importance appear the pronounced peaks in the vicinity of $E_F + 2\hbar\omega$ and, in particular, $E_F + 4\hbar\omega$. These broad peaks can act as doorway states resonantly enhancing multiphoton emission compared to the prediction of the jellium model. Their presence supports the quantum-pathway interference model for reaching the short-lived resonance at $E_F + 4\hbar\omega$, from where photoemission proceeds.

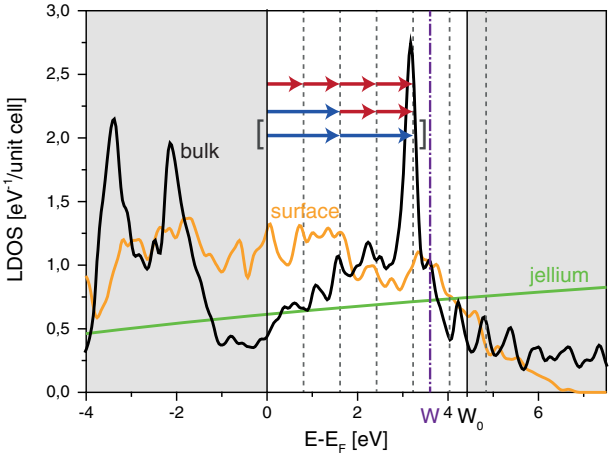

FIG. 4. Local density of states (LDOS) from a ground-state slab calculation (20 layers) for W(310). LDOS at surface (labeled surface, orange line), LDOS for jellium (labeled jellium, green line), and, for comparison, DOS from a bulk calculation (labeled bulk, black line). Intermediate surface and volume states are found at $2\hbar\omega = 1.6$ eV and $4\hbar\omega = 3.2$ eV. Three pathways to an energy of $E_F + 4\hbar\omega$ are indicated. The two-photon pathway is negligible under our conditions because of the small 2ω intensity. The reduction of the work function due to the bias voltage is indicated by the purple dash-dotted line at 3.6 eV.

The lifetime of excited states is limited by their spectral width, by the presence of the optical field, which ionizes them, and by diffusion of the electron to the bulk. From our experiment we can determine an upper bound for the lifetime of involved intermediate states to be less than 10 fs. This can be concluded from the full width at half maximum of the photocurrent components, which are (78 ± 10) fs for ROI 0 and (84 ± 10) fs for ROI 1, determined from the Gaussian fits to the data in Fig. 2. These are slightly shorter than the expected cooperative signals from a convolution of the laser pulses for all applied intensities. The symmetry of the photocurrent components of ROI 0 and ROI 1 as a function of the pulse delay is another indicator of a short lifetime.

In summary, we have demonstrated quantum-pathway interference in multiphoton and above-threshold photoemission at a tungsten tip on femtosecond time scales with two-color femtosecond driving fields. Despite the solid-state nature of the emitter, the maximum modulation depth of 94% is, to the best of our knowledge, the highest reported value for two-color photoemission experiments, including those for isolated atoms in the gas phase [42]. This high visibility is closely related to the nanometer-sized interaction volume, preventing the influence of focal averaging effects and inhomogeneous broadening. Nanotips may therefore be used as nanometric probes to measure light phases [43]. Moreover, we have demonstrated a potential building block for the development of light wave electronics [44] on the femtosecond duration and nanometer length scales.

Additionally, we expect that polarization-shaped [45] two-color laser pulses together with the polarization-sensitive near-field distribution [41], the spatially dependent work function on the nanometer scale, and the Gouy phase shift will permit engineered spatiotemporal electron emission profiles at single tips and tip arrays, highly desired for use in electron guns for coherent x-ray generation [25].

This project was funded in part by the ERC grant "Near Field Atto," by DFG SPP 1840 "QUTIF," and by the Austrian Science Fund (FWF) within the special research projects SFB-041 "ViCoM," SFB-049 "Next Lite," and Project No. P21141-N16. M. F. and G. W. acknowledge support by the IMPRS-APS. We thank Sebastian Thomas for supporting FDTD simulations, Alexander Lang for contributions to the experimental setup, and Misha Yu. Ivanov, Thomas Fauster, Martin Hundhausen, and Takuya Higuchi for helpful discussions. Simulations were performed in part on the Vienna Scientific Cluster (VSC).

*michael.foerster@fau.de
†Present address: Weizmann Institute of Science, 234 Herzl Street, Rehovot 7610001, Israel.

[1] H. G. Muller, P. H. Bucksbaum, D. W. Schumacher, and A. Zavriyev, Above-threshold ionisation with a two-colour laser field, J. Phys. B **23**, 2761 (1990).
[2] D. W. Schumacher, F. Weihe, H. G. Muller, and P. H. Bucksbaum, Phase Dependence of Intense Field Ionization: A Study Using Two Colors, Phys. Rev. Lett. **73**, 1344 (1994).
[3] F. Ehlotzky, Atomic phenomena in bichromatic laser fields, Phys. Rep. **345**, 175 (2001).
[4] B. Sheehy, B. Walker, and L. F. DiMauro, Phase Control in the Two-Color Photodissociation of HD^+, Phys. Rev. Lett. **74**, 4799 (1995).
[5] M. R. Thompson, M. K. Thomas, P. F. Taday, J. H. Posthumus, A. J. Langley, L. J. Frasinski, and K. Codling, One and two-colour studies of the dissociative ionization and Coulomb explosion of H_2 with intense Ti:sapphire laser pulses, J. Phys. B **30**, 5755 (1997).
[6] H. Ohmura, T. Nakanaga, and M. Tachiya, Coherent Control of Photofragment Separation in the Dissociative Ionization of IBr, Phys. Rev. Lett. **92**, 113002 (2004).
[7] M. Fifirig, A. Cionga, and F. Ehlotzky, Elliptic dichroism in hydrogen ionization by a coherent superposition of two harmonics, Eur. Phys. J. D **23**, 333 (2003).
[8] A. Cionga, M. Fifirig, and F. Ehlotzky, Dichroic effects in the two-colour, two-photon ionization of hydrogen, J. Mod. Opt. **50**, 615 (2003).
[9] S. De, I. Znakovskaya, D. Ray, F. Anis, N. G. Johnson, I. A. Bocharova, M. Magrakvelidze, B. D. Esry, C. L. Cocke, I. V. Litvinyuk, and M. F. Kling, Field-Free Orientation of CO Molecules by Femtosecond Two-Color Laser Fields, Phys. Rev. Lett. **103**, 153002 (2009).
[10] X. Xie, S. Roither, D. Kartashov, E. Persson, D. G. Arbó, L. Zhang, S. Gräfe, M. S. Schöffler, J. Burgdörfer, A. Baltuška, and M. Kitzler, Attosecond Probe of Valence-Electron Wave Packets by Subcycle Sculpted Laser Fields, Phys. Rev. Lett. **108**, 193004 (2012).
[11] D. G. Arbó, S. Nagele, X.-M. Tong, X. Xie, M. Kitzler, and J. Burgdörfer, Interference of electron wave packets in atomic ionization by subcycle sculpted laser pulses, Phys. Rev. A **89**, 043414 (2014).
[12] D. G. Arbó, The effect of the Coulomb potential on subcycle interference of electron wave packets in atomic ionization by two-colour laser pulses, J. Phys. B **47**, 204008 (2014).
[13] J. C. H. Spence, *High-Resolution Electron Microscopy*, 4th ed. (Oxford University Press, New York, 2013).
[14] D. Ehberger, J. Hammer, M. Eisele, M. Krüger, J. Noe, A. Högele, and P. Hommelhoff, Highly Coherent Electron Beam from a Laser-Triggered Tungsten Needle Tip, Phys. Rev. Lett. **114**, 227601 (2015).
[15] L. Novotny and B. Hecht, *Principles of Nano-Optics*, 2nd ed. (Cambridge University Press, Cambridge, 2012).
[16] R. Bormann, M. Gulde, A. Weismann, S. V. Yalunin, and C. Ropers, Tip-Enhanced Strong-Field Photoemission, Phys. Rev. Lett. **105**, 147601 (2010).
[17] M. Schenk, M. Krüger, and P. Hommelhoff, Strong-Field Above-Threshold Photoemission from Sharp Metal Tips, Phys. Rev. Lett. **105**, 257601 (2010).
[18] M. Krüger, M. Schenk, and P. Hommelhoff, Attosecond control of electrons emitted from a nanoscale metal tip, Nature (London) **475**, 78 (2011).
[19] M. Krüger, M. Schenk, P. Hommelhoff, G. Wachter, C. Lemell, and J. Burgdörfer, Interaction of ultrashort laser pulses with metal nanotips: a model system for strong-field phenomena, New J. Phys. **14**, 085019 (2012).
[20] G. Herink, D. R. Solli, M. Gulde, and C. Ropers, Field-driven photoemission from nanostructures quenches the quiver motion, Nature (London) **483**, 190 (2012).
[21] B. Piglosiewicz, S. Schmidt, D. J. Park, J. Vogelsang, P. Groß, C. Manzoni, P. Farinello, G. Cerullo, and C. Lienau, Carrier-envelope phase effects on the strong-field photoemission of electrons from metallic nanostructures, Nat. Photonics **8**, 37 (2014).
[22] P. Hommelhoff and M. Kling, *Attosecond Nanophysics* (Wiley-VCH, Weinheim, 2015).
[23] M. Gulde, S. Schweda, G. Storeck, M. Maiti, H. K. Yu, A. M. Wodtke, S. Schäfer, and C. Ropers, Ultrafast low-energy electron diffraction in transmission resolves polymer/graphene superstructure dynamics, Science **345**, 200 (2014).
[24] M. Müller, A. Paarmann, and R. Ernstorfer, Femtosecond electrons probing currents and atomic structure in nanomaterials, Nat. Commun. **5**, 5292 (2014).
[25] W. S. Graves, F. X. Kärtner, D. E. Moncton, and P. Piot, Intense Superradiant X Rays from a Compact Source Using a Nanocathode Array and Emittance Exchange, Phys. Rev. Lett. **108**, 263904 (2012).
[26] P. M. Nagel, J. S. Robinson, B. D. Harteneck, T. Pfeifer, M. J. Abel, J. S. Prell, D. M. Neumark, R. A. Kaindl, and S. R. Leone, Surface plasmon assisted electron acceleration in photoemission from gold nanopillars, Chem. Phys. **414**, 106 (2013).
[27] M. E. Swanwick, P. D. Keathley, A. Fallahi, P. R. Krogen, G. Laurent, J. Moses, F. X. Kärtner, and L. F. Velásquez-García, Nanostructured Ultrafast Silicon-Tip Optical Field-Emitter Arrays, Nano Lett. **14**, 5035 (2014).
[28] M. U. Wehner, M. H. Ulm, and M. Wegener, Scanning interferometer stabilized by use of Pancharatnam's phase, Opt. Lett. **22**, 1455 (1997).

[29] E. W. Müller, Work Function of Tungsten Single Crystal Planes Measured by the Field Emission Microscope, J. Appl. Phys. **26**, 732 (1955).
[30] E. W. Müller, Field Ion Microscopy, Science **149**, 591 (1965).
[31] See Supplemental Material at http://link.aps.org/supplemental/10.1103/PhysRevLett.117.217601, which includes Refs. [32–38], for details on the experimental setup, the data analysis, and the simulation methods.
[32] M. Klein and G. Schwitzgebel, An improved lamellae drop-off technique for sharp tip preparation in scanning tunneling microscopy, Rev. Sci. Instrum. **68**, 3099 (1997).
[33] M. Krüger, S. Thomas, M. Förster, and P. Hommelhoff, Self-probing of metal nanotips by rescattered electrons reveals the nano-optical near-field, J. Phys. B **47**, 124022 (2014).
[34] E. E. Martin, F. M. Charbonnier, W. W. Dolan, W. P. Dyke, H. W. Pitman, and J. K. Trolan, Research on Field Emission Cathodes, Wright Air Development Division, Technical Report 59-20 (1960).
[35] J. Zuber, K. L. Jensen, and T. E. Sullivan, An analytical solution for microtip field emission current and effective emission area, J. Appl. Phys. **91**, 9379 (2002).
[36] G. L. Yudin and M. Y. Ivanov, Nonadiabatic tunnel ionization: Looking inside a laser cycle, Phys. Rev. A **64**, 013409 (2001).
[37] G. Kresse and J. Furthmüller, Efficiency of ab-initio total energy calculations for metals and semiconductors using a plane-wave basis set, Comput. Mater. Sci. **6**, 15 (1996).
[38] J. P. Perdew, K. Burke, and M. Ernzerhof, Generalized Gradient Approximation Made Simple, Phys. Rev. Lett. **77**, 3865 (1996).
[39] S. Thomas, M. Krüger, M. Förster, M. Schenk, and P. Hommelhoff, Probing of Optical Near-Fields by Electron Rescattering on the 1 nm Scale, Nano Lett. **13**, 4790 (2013).
[40] S. Thomas, G. Wachter, C. Lemell, J. Burgdörfer, and P. Hommelhoff, Large optical field enhancement for nanotips with large opening angles, New J. Phys. **17**, 063010 (2015).
[41] H. Yanagisawa, C. Hafner, P. Doná, M. Klöckner, D. Leuenberger, T. Greber, M. Hengsberger, and J. Osterwalder, Optical Control of Field-Emission Sites by Femtosecond Laser Pulses, Phys. Rev. Lett. **103**, 257603 (2009).
[42] P. Ackermann, A. Scharf, and T. Halfmann, Strong quantum interferences in frequency up-conversion towards short vacuum-ultraviolet radiation pulses, Phys. Rev. A **89**, 063804 (2014).
[43] C. Chen and D. S. Elliott, Measurements of optical phase variations using interfering multiphoton ionization processes, Phys. Rev. Lett. **65**, 1737 (1990).
[44] F. Krausz and M. I. Stockman, Attosecond metrology: from electron capture to future signal processing, Nat. Photonics **8**, 205 (2014).
[45] T. Brixner and G. Gerber, Femtosecond polarization pulse shaping, Opt. Lett. **26**, 557 (2001).